Ridge reflection of surface plasmon-polaritons in a one-dimensional plasmonic cavity

Keisuke Ozawa and Naoki Yamamoto
Department of Materials Science and Engineering, Tokyo Institute of Technology, Midori-ku, Yokohama 226–8503, Japan

(Received 21 December 2018; published 2 August 2019)

Reflection characteristics of surface plasmon polariton (SPP) by a rectangular ridge on the silver surface were examined theoretically and experimentally. The amplitude and phase shift of the SPP reflection by the rectangular ridge were calculated by SPP scattering theory using Green's tensor method and expressed in terms of ridge width and SPP energy. It was found that this calculation result can be reproduced well by a simple model expressed by superposition of reflections by the two steps constituting the ridge. A one-dimensional cavity composed of a pair of rectangular ridges was fabricated, and the characteristics of the SPP standing wave mode (cavity mode) was clarified for the first time using the scanning transmission electron microscope (STEM) - cathodoluminescence (CL) method and was used to evaluate the theoretical calculations of the reflection coefficient. The cavity mode energies are derived from the angle-resolved spectral (ARS) pattern, and the phase shift of the SPP reflection can be deduced through the cavity condition. We successfully explained the resonance energy of the cavity mode and the spatial distribution of the SPP standing wave by using the SPP reflection coefficient of the rectangular ridge derived by the theory.

DOI: 10.1103/PhysRevB.100.075406

I. INTRODUCTION

Surface plasmon polariton (SPP) is a longitudinal electromagnetic wave mode propagating at the interface between metal and dielectric (vacuum). SPP combines with photons due to surface irregularities such as steps and ridges, and a part of it is released as light into free space [1,2]. Various applications have been proposed utilizing the properties of SPP such as surface localization and field enhancement to plasmonic laser [3], plasmonic cavity [4] nanophotonics [5,6], etc. It is important to elucidate basic characteristics of the interaction between SPP and light through such surface nanostructures in plasmonics technology aiming for application to SPP cavity and waveguides. Experimental and theoretical studies on the reflection and light emission of SPP due to the nanostructure of the metal surface have been conducted with the surface protrusions [7], surface steps [8–10], ridges, and grooves [11–16]. However, even for basic structures such as rectangular ridges and rectangular grooves, only few studies have systematically investigated the shape and size dependence of reflection and light emission efficiency. The reason for this is that the experimental method that can excite SPP and detect simultaneously emitted light is limited.

We have developed a cathodoluminescence (CL) method using a scanning transmission electron microscope (STEM) [10,17] as a powerful experimental method to observe SPP-light conversion by surface nanostructures. A high-energy electron accelerated in STEM excites SPP together with transition radiation when incident on the metal surface. Light converted from SPP by surface nanostructure is detected by the CL system and spectroscopic analysis is successively performed. Recently, angle-resolved measurements have become possible by combining a parabolic mirror for light collection and a pinhole mask. We have applied this technique to single step [9,10], plasmonic crystal [18–20], cavity in plasmonic crystal [21–23], and waveguide [24], and studied the properties of SPPs peculiar to these structures from angle-resolved measurements of light. The STEM-CL method typically provides an angle-resolved spectral (ARS) pattern by moving a pinhole mask, and also a beam-scan spectral (BSS) image produced from the radiation spectra recorded while scanning an electron beam.

In this study, we treat a rectangular ridge as a typical surface nanostructure. Then we examine a cavity which is composed of a pair of parallel ridges. Such cavities resonate strongly when the ridge has a larger SPP reflectance. Therefore, to design an efficient one-dimensional (1D) plasmon cavity, information on the SPP reflection coefficient (amplitude and phase shift) is important. The cavity can be designed to resonate well at the required wavelength by providing the reference data of the SPP reflection coefficient depending on the shape of the ridge and wavelength (or energy). However, the SPP reflection coefficient by the ridge depends complicatedly on ridge shape and energy, and there are few studies systematically investigated so far. We applied the STEM-CL method to this cavity structure for the first time, and experimentally clarified the characteristics of the cavity composed of the rectangular ridges with various widths from the analysis of the ARS pattern and the BSS image.

Here we consider the case that SPP propagates perpendicular to the ridge of the cavity and is radiated to the direction in the two-dimensional plane subtended by the surface normal direction and that normal to the ridge. The paper is organized as follows. In Sec. II, the reflection coefficient $Re^{i\phi}$ of SPP by a single rectangular ridge is derived from the SPP scattering theory using the Green's tensor method, and the dependence on the ridge width w and the energy E is shown. In Sec. III, in order to physically understand the dependence of R and ϕ on w and E, we propose a simple model that approximates the theoretically obtained reflection coefficient in Sec. II. Next,

we fabricate a cavity in which two ridges are arranged in parallel on the silver surface, and investigate the property of radiation from the cavity by the STEM-CL method. In Sec. IV, we briefly describe the sample of cavity and the experimental arrangement used in the STEM-CL. In Sec. V, we use an approximation to replace the ridge with a single wall of reflection coefficient $Re^{i\phi}$ and derive an equation which presents the angular distribution of the radiation from the cavity. Here, the cavity length is L, and the SPP standing wave of the mode n formed in the cavity has a wave number k_p satisfying the following resonance condition [21,25]:

$$k_p L + \phi = n\pi, \tag{1}$$

where the wave number can be derived from the dispersion relation of SPP propagating on a flat silver surface, i.e., $k_p = (E/\hbar c)\sqrt{\varepsilon(E)/(\varepsilon(E)+1)}$, and mutually converts with SPP energy. That is, the resonance energy of the cavity is directly related to the phase shift ϕ of the reflection coefficient by Eq. (1). Here, ε (E) is the dielectric function of silver, $\hbar$ is the Planck's constant divided by 2π, and c is the velocity of light in vacuum. In the ARS pattern, a characteristic radiation distribution appears at the position of the energy satisfying Eq. (1), so that the energy dependence of the phase shift ϕ can be derived using Eq. (1) and compared with the theoretical one. The BSS image directly visualizes the SPP standing waves in the cavity, and the magnitude R of the reflection coefficient can be estimated from the intensity. From these results, we check the validity of applying the SPP reflection coefficient to explain the radiative properties of the cavity consisting of the ridge pair. Finally, we summarize the main conclusions in Sec. VI.

II. THEORY OF SPP REFLECTION BY RECTANGULAR RIDGE

Reflection and radiation of SPP by a rectangular ridge on a metal surface were recently treated theoretically by Brucoli and Martin-Moreno [15,16]. They calculated the transmittance, reflectance and radiation of SPP by the ridge as a function of wavelength when the SPP is incident perpendicularly on the rectangular ridge for some shape parameters (ridge width, ridge height). However, since the phase shift of reflected SPP has not been investigated, it is difficult to deal with the resonance property of cavities composed of the rectangular ridge. Here we examine in detail how the reflection coefficient of the SPP due to the rectangular ridge changes with respect to the ridge width and the SPP energy. The calculated reflection coefficient is used for analysis of the cavity radiation observed by the STEM-CL method.

We calculated the amplitude and phase shift of SPP reflection by rectangular ridges using the Green's tensor method [26,27]. Assuming that the direction perpendicular to the rectangular ridge is the x axis and the direction perpendicular to the surface is the z axis, SPP wave vector $\boldsymbol{k}_p$ and position coordinates are all treated as a two-dimensional problem on the $x-z$ plane. As shown in Fig. 1(a), a space of an appropriate size is divided into sufficiently small cells, and positions are designated by consecutive numbers from 1 to N. Given the background field E_b in the background medium of the dielectric function ε_b, the μ component of the scattered

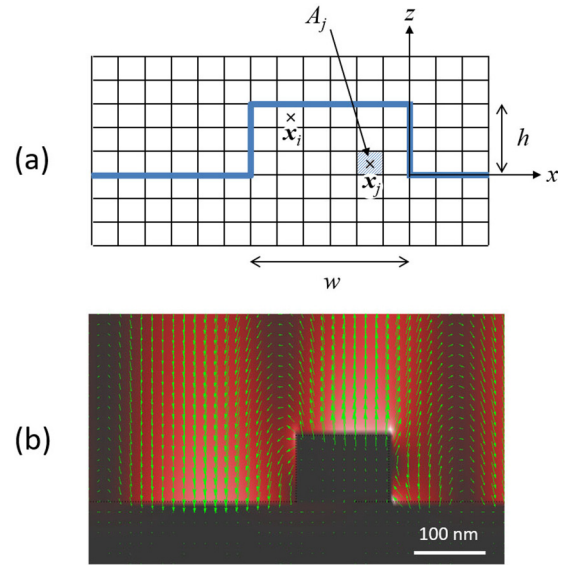

FIG. 1. Discretization of an area containing a rectangular ridge for the calculation of SPP reflection coefficient.

electric field E on a silver surface with a silver ridge of the dielectric function $\varepsilon = \varepsilon_\mathrm{b} + \Delta\varepsilon$ is calculated by the discretized Lippmann-Schwinger equation:

$$\begin{aligned} E_\mu(\boldsymbol{x}_i) = E_{\mathrm{b},\,\mu}(\boldsymbol{x}_i) &+ k_0^2 \sum_{j\neq i}\sum_{\nu} G_{0,\mu\nu}(\boldsymbol{x}_i - \boldsymbol{x}_j)\Delta\varepsilon E_\nu(\boldsymbol{x}_j)A_j \\ &+ k_0^2 \sum_{\nu} M_{\mu\nu}\Delta\varepsilon E_\nu(\boldsymbol{x}_j) - \sum_{\nu}\frac{L_{\mu\nu}}{\varepsilon_\mathrm{b}}\Delta\varepsilon E_\nu(\boldsymbol{x}_j) \\ &+ k_0^2 \sum_{j}\sum_{\nu} G_{\mathrm{R},\mu\nu}(\boldsymbol{x}_i - \boldsymbol{x}_j)\Delta\varepsilon E_\nu(\boldsymbol{x}_j)A_j, \end{aligned} \tag{2}$$

where the suffix indicates the cell number $(i,\ j = 1, 2, \cdots, N)$, A_j is the area of the jth cell, k_0 is the wave number in the air, G_0 and G_R are the homogeneous and reflected Green's tensors, $(L_{\mu\nu})$ and $(M_{\mu\nu})$ are the polarization tensor and its compensative tensor for the discretized Lippmann-Schwinger equation $(\mu, \nu = x, z)$. The tensor $(L_{\mu\nu})$ has elements of $L_{\mu\nu} = \delta_{\mu\nu}/3$ for square lattices [27].

G_0 and G_R are obtained by using the SPP field on the metal surface as the background field [27]. By sequentially calculating the scattering field and the Green's tensor at each cell, a scattering field due to the entire ridge can be obtained. We approximated the scattering field using an iterative algorithm [28,29]. First, we rewrite Eq. (2) using $G^{(0)} = G_0 + G_\mathrm{R}$ and obtain

$$E_\mu^{(k)} = E_\mu^{(k-1)} + \sum_{\nu} G_{\mu\nu;il_k}^{(k-1)} V_{l_k} A_{l_k} E_{\nu l_k}^{(k)}. \tag{3a}$$

The scattering field and the Green's tensor were iteratively calculated over all lattice points labeled l_k $(l_k = 1,\ 2, \cdots, N)$ as

$$G_{\mu\nu;ij}^{(k)} = G_{\mu\nu;ij}^{(k-1)} + \sum_{\xi} G_{\mu\nu;il_k}^{(k-1)} V_{l_k} A_{l_k} G_{\mu\nu;l_k j}^{(k)}. \tag{3b}$$

Here, V_{l_k} is a potential represented by $V_{l_k} = k_0^2\Delta\varepsilon(\boldsymbol{x}_{l_k})$. Equations (3a) and (3b) can be solved algebraically in an

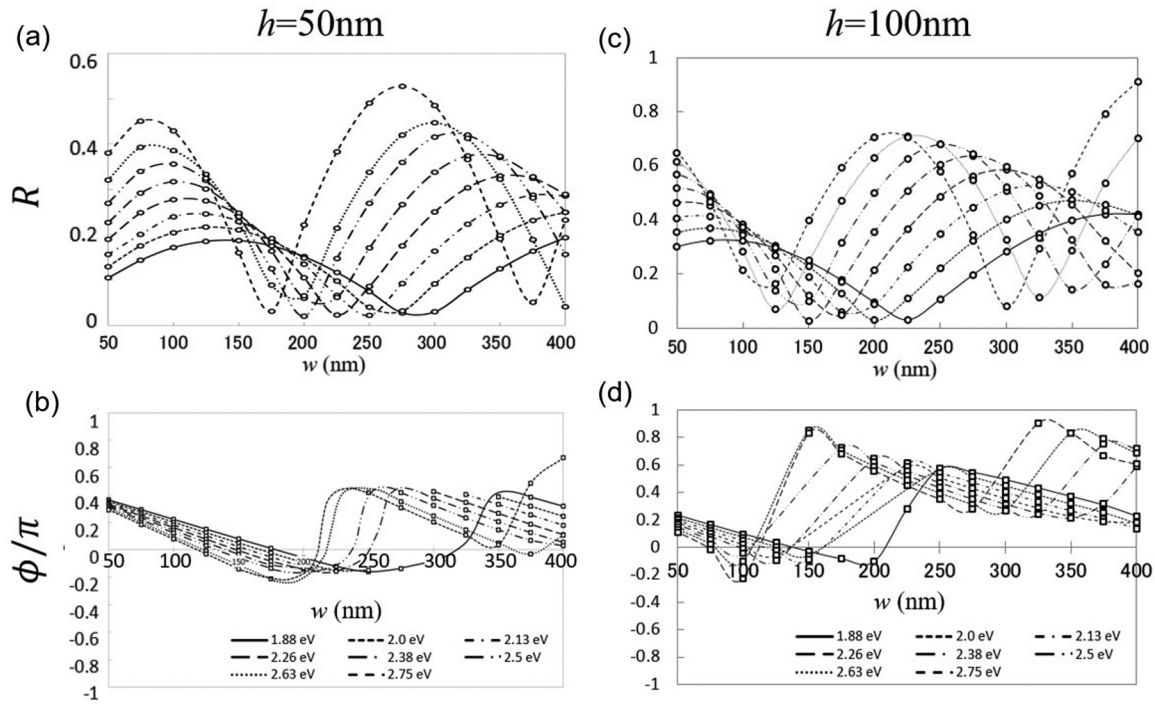

FIG. 2. Amplitude R and phase shift ϕ of the reflection coefficient of SPP as a function of ridge width w calculated for various energies: [(a) and (b)] ridge height of $h = 50$ nm and [(c) and (d)] $h = 100$ nm.

incremental manner of k, and the scattering field is approximately obtained.

For the calculation of the reflected SPP, we used the fact that the Green's tensor represents the excitation of the backward SPP at the poles $k_x = -k_{px}$ as dealt with in Ref. [27]. We can obtain the reflected SPP by summing all the excitations from the polarization $\boldsymbol{P} = \Delta\varepsilon\boldsymbol{E}$ in the ridge of the height h and width w placed under the already calculated scattering field, as shown in the following equation:

$$\boldsymbol{E}_p^{(\mathrm{R})}(\boldsymbol{x}) = \frac{-\varepsilon\sqrt{\varepsilon}}{(1-\varepsilon^2)k_0^2} \sum_{\boldsymbol{x}_j \text{ in ridge}} e^{i\{-k_{px}(x-x_j)+k_{pz}(z+z_j)\}} \times \begin{pmatrix} (k_{pz})^2 & k_{pz}k_{px} \\ -k_{pz}k_{px} & -|k_{px}|^2 \end{pmatrix} \Delta\varepsilon A_j \boldsymbol{E}(\boldsymbol{x}_j). \quad (4)$$

The incident SPP and the reflection SPP are in the form of $e^{i(k_{px}x+k_{pz}z)}$ and $Re^{i\phi}e^{i(-k_{px}x+k_{pz}z)}$, and the amplitude R and phase shift ϕ of the reflection coefficient were calculated by setting the origin of the x-axis at the outer end of the ridge. Figure 1(b) shows, as an example, the electric field distribution calculated for a ridge width of 150 nm and a ridge height of 100 nm at 1.88 eV. In the calculation we take an area of 800 nm × 400 nm and a cell size of 16 nm square, and then the total number of cells is $N = 1250$. It is seen that the antinode of the SPP produced by the interference between the incident SPP and the reflection SPP is located near the outer end of the ridge but slightly shifted from there.

The dependence of SPP reflection coefficient on the rectangular ridge width was investigated from calculation by the theory. The size of the discretization cell was set to 5 nm square and the total number of cells $N = 12800$. The ridge width was varied from 50 nm to 400 nm at a fixed height of 50 nm in steps of 25 nm for calculation. The range of SPP energy was selected according to the experiment. For calculation, we refer to the optical constants of silver by Johnson and Christy [30]. Figures 2(a) and 2(b) show the dependence of R and ϕ on the ridge width w calculated with several energies from 1.88 eV to 2.75 eV. The amplitude R in this energy range becomes maximum at $w = 100$ to 150 nm and $w = 300$ to 400 nm, and becomes minimum around $w = 200$ nm. The maximum value of R increases as the energy of SPP increases. The phase shift ϕ decreases with increasing w, but it changes abruptly near $w = 200$ to 250 nm where R is minimized. Both amplitude and phase shift oscillate quasiperiodically as the ridge width increases. Figures 2(c) and 2(d) show the dependence of R and ϕ when the ridge height is 100 nm. Comparing the curves of the same energy for the amplitude R in Figs. 2(a) and 2(c), R is larger when $h = 100$ nm, and the maximum and minimum positions are shifted to the smaller w. Similarly, it can be seen from Figs. 2(b) and 2(d) that the phase shift ϕ also oscillates more largely at $h = 100$ nm, and the curve of ϕ of the same energy shifts to the smaller side of w.

III. SIMPLE MODEL OF SPP REFLECTION BY RECTANGULAR RIDGE

We propose a simple model to understand intuitively the dependence of the amplitude R and the phase shift ϕ on the ridge width w shown in Fig. 2. As schematically shown in Fig. 3, the reflection due to the rectangular ridge is represented by the interference of the reflected waves of the SPP by the two steps. Let $r_u e^{i\phi_u}$ and $r_d e^{i\phi_d}$ be the reflection coefficients of the up step at the front side of the rectangular ridge and the down step at the outer end, respectively. The reflection

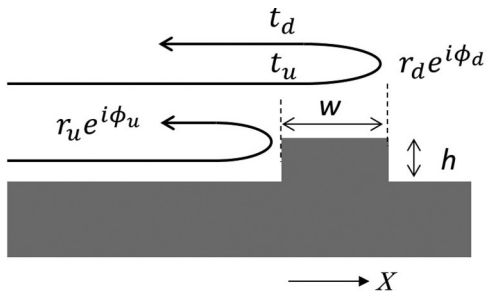

FIG. 3. Reflection model of SPP by rectangular ridge.

coefficient of the ridge is expressed as

$$Re^{i\phi} = r_u e^{i(\phi_u - 2k_p w)} + t_u t_d r_d e^{i\phi_d} / \left(1 - {r_d}^2 e^{i(2\phi_d + 2k_p w)}\right). \quad (5)$$

The position of the down step is taken as a reference of the phase of the reflected wave as in the previous section. Therefore the phase difference $-2k_p w$ is added to the phase of the reflected wave of the up step with respect to the down step. In addition, t_u and t_d are the transmission coefficients for the SPP crossing the up step from left to right and vice versa, respectively. The last factor in the second term of Eq. (5) represents the effect of multiple reflection of SPP on the ridge. Equation (5) shows that the reflection coefficient of a specific energy E oscillates with respect to w, and its period becomes $2\pi/2k_p(E) = \lambda_p/2$.

Figure 4(a) shows the relation between the ridge width w and the energy, which gives the maximum and the minimum reflection amplitude (R), extracted from the calculated result of Fig. 2(a). Our preliminary experiments of the reflection of SPP by a single step suggested that up step approximately acts as a fixed end ($\phi_u \sim \pi$) and down step acts as an open end ($\phi_d \sim 0$). As schematically shown in Figs. 4(b) and 4(d), when the ridge width w is $\lambda_p/4$ and $3\lambda_p/4$, the reflected waves by the two steps are in phase. Therefore it is expected that the reflected waves cooperatively interfere with each other and R becomes large. On the other hand, when w is $\lambda_p/2$, the phases of the two reflected waves differ by π as shown in Fig. 4(c), so that the two waves distractively interfere so as to cancel each other, and R becomes minimum. The relation between the ridge width and energy expected from this simple consideration is represented by the solid lines in Fig. 4(a) using the dispersion relation of SPP on silver surface.

The ridge width giving the theoretically calculated maximum and minimum R shows the w dependence similar to the simple model in the whole energy range of the figure, but its value is about 40 nm smaller than the solid line. This indicates that the up and down steps at both ends of the ridge do not act as perfectly fixed end and open end, respectively, i.e., ϕ_u and ϕ_d deviate from π and 0. Furthermore, as shown in Fig. 2, the position of w at which R becomes maximum or minimum also depends on the ridge height. Figure 2 shows that the curves of R and ϕ shifts to the smaller w as a whole when the ridge height increases from 50 to 100 nm. This behavior can be expressed by replacing the first term of Eq. (5) with $r_u \exp[i\{\phi_u - 2k_p(w + \eta h)\}]$. Here, η is a fitting parameter taking a value between 0.0 and 1.0.

Here we describe how to select parameters that approximate the calculation results of the amplitude and phase shift of the ridge at $h = 50$ nm [Figs. 2(a) and 2(b)]. Since the minimum value of R is close to 0, the amplitudes of r_u and $t_u t_d r_d$ should have nearly the same values. Also, from the maximum value of R, it is required that their values should be around 0.2 to 0.25. Regarding the phase, we started from $\phi_u = \pi$ and $\phi_d = 0$, and changed them until they approached the proper values to reproduce the theoretical curves in Fig. 2. These phases make the curve in Fig. 2(b) to shift in the vertical direction. Furthermore, the parameter η and

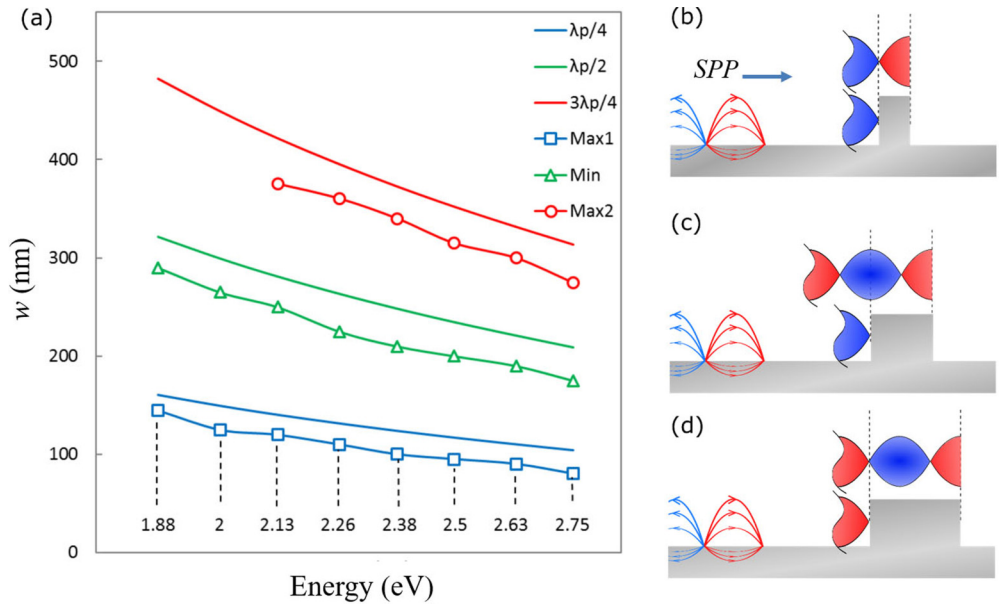

FIG. 4. (a) Relation between ridge width and energy giving maximum and minimum reflection amplitude ($h = 50$ nm): Plots are extracted from the calculated values in Fig. 3, and solid lines indicate $\lambda_p/4$, $\lambda_p/2$, and $3\lambda_p/4$ lines against energy. [(b)–(d)] Schematic diagram of the SPP reflection by ridges of various widths; (b) $D = \lambda_p/4$, (c) $D = \lambda_p/2$, and (d) $D = 3\lambda_p/4$.

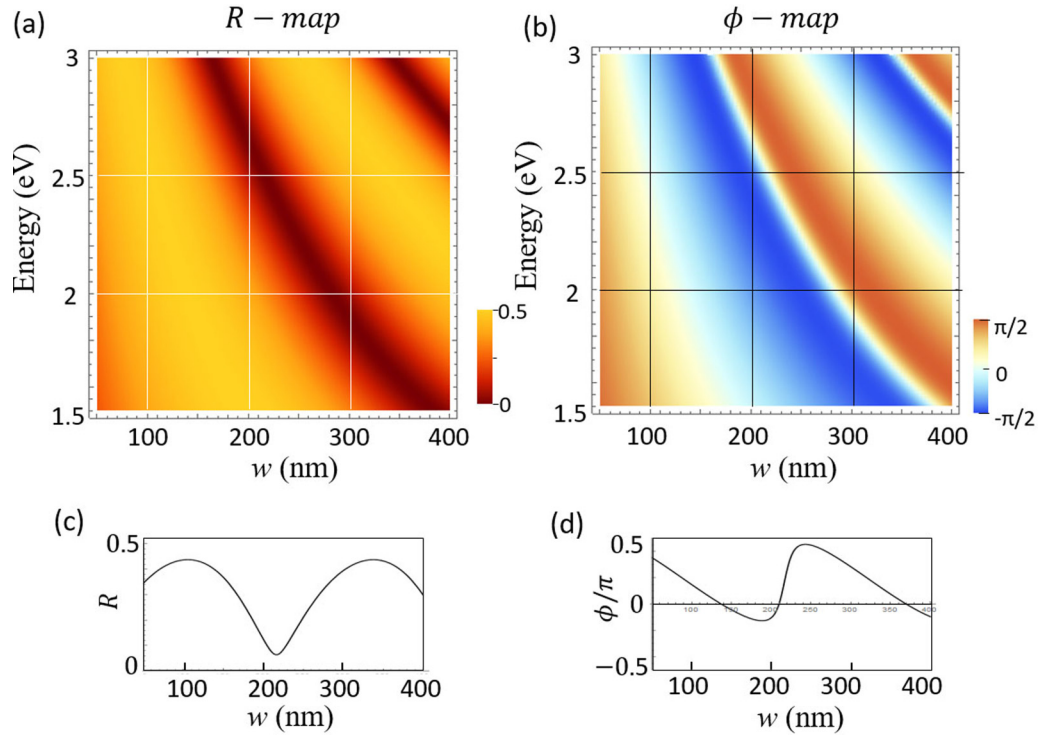

FIG. 5. (a) Amplitude R and (b) phase shift ϕ of the reflection coefficient of a rectangular ridge with a height of 50 nm calculated using $(Re^{i\phi})_{h=50}$. [(c) and (d)] Profiles of $R(w)$ and $\phi(w)$ at energy of 2.5 eV, respectively.

the phase difference between ϕ_u and ϕ_d shift the curve in Figs. 2(a) and 2(b) in the horizontal direction. These parameters were adjusted so as to reproduce all the theoretical curves in Figs. 2(a) and 2(b). In addition the wave number k_p of SPP was approximated by a function of energy E derived from the dispersion relation using the optical constant data of silver by Johnson and Christy [30], though its imaginary part is very small in the relevant energy range.

Finally, the reflection coefficient of the ridge at $h = 50$ nm [Figs. 2(a) and 2(b)] is qualitatively well reproduced by setting $r_u = 0.2$, $\phi_u = 1.15\pi$, $t_u t_d r_d = 0.25$, $\phi_d = 0.15\pi$, and $\eta = 0.3$ in Eq. (5). Here we simply denote this function as $(Re^{i\phi})_{h=50}$. It is difficult to match the theoretical curves accurately over a wide range of w and E because the theoretical curve is not a periodic function, and some deviation occurs near the region where the phase shift changes rapidly. A two-dimensional maps representing $R(E, w)$ and $\phi(E, w)$ calculated using $(Re^{i\phi})_{h=50}$ are shown in Figs. 5(a) and 5(b), respectively. Figures 5(c) and 5(d) show the profiles of R and ϕ as a function of w at $E = 2.5$ eV for comparison with the curves in Figs. 2(a) and 2(b). Next, the reflection coefficient of the ridge with $h = 100$ nm [Figs. 2(c) and 2(d)] is well reproduced by setting $r_u = 0.3$, $\phi_u = 1.15\pi$, $t_u t_d r_d = 0.35$, $\phi_d = 0.15\pi$, and $\eta = 1.0$, which is denoted as $(Re^{i\phi})_{h=100}$. In addition, we prepare the reflection coefficient $(Re^{i\phi})_{h=70}$ of the ridge with $h = 70$ nm because it will be needed for simulation in the later section. Unfortunately, we did not calculate it by the theory, but it is expected that $(Re^{i\phi})_{h=70}$ can be roughly approximated by interpolating between $(Re^{i\phi})_{h=50}$ and $(Re^{i\phi})_{h=100}$. Then we set the parameters for $(Re^{i\phi})_{h=70}$ as $r_u = 0.25$, $t_u t_d r_d = 0.3$, $\eta = 0.6$ and with the same values of ϕ_u and ϕ_d. We will use these reflection coefficients, $(Re^{i\phi})_{h=50}$ and $(Re^{i\phi})_{h=70}$, for the simulations in the later section.

IV. ANGLE-RESOLVED MEASUREMENT OF 1D-CAVITY BY STEM-CL

The properties of radiation from a cavity consisting of two rectangular ridges were investigated by the STEM-CL method. The experimental setup is schematically shown in Fig. 6. The details of the angle-resolved CL experiment with STEM are described in our previous paper [10,17]. For the cavity sample, a pair of rectangular ridges of width (w) were arranged in parallel at a distance (d). Ridge height was set to $h = 50$ or 70 nm, and ridge length 50 μm. Here, the cavity length (L) is defined by the interval between the outer down steps of the cavity, i.e., $L = d + 2w$. Cavity samples

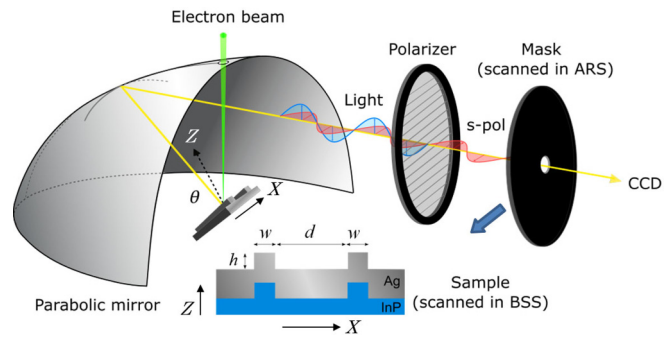

FIG. 6. Setup of angle-resolved measurement using a parabolic mirror.

were prepared on InP substrates by electron beam lithography and coated with 200-nm-thick silver layer. The sample was scanned with an electron beam having energy of 200 keV and a probe size of about 10 nm using a STEM (JEM2000FX). The cavity length was measured from SEM mode observation of the STEM. An electron beam irradiating inside the cavity excites an SPP and forms an SPP standing wave of a specific energy satisfying the cavity condition. The SPP standing wave is converted into light by ridges on both sides of the cavity. The STEM-CL measurement was performed to provide the angle-resolved spectral (ARS) pattern and the beam scanning spectral (BSS) image. In the measurement of the ARS pattern, the emission spectrum of s polarized light was recorded with moving a pinhole mask horizontally while scanning the electron beam over the inner flat region (width d) in the cavity. The diameter of the pinhole is 0.5 mm, which corresponds to 1.2×10^{-2} str in the surface normal direction. In the measurement of the BSS image, the emission spectrum of s polarized light was recorded while moving an electron beam across the cavity with the pinhole fixed.

In the STEM-CL measurement, a sample is placed at the focal position of the parabolic mirror inside the STEM (Fig. 6) so that the rectangular ridge is parallel to the axial direction of the parabolic surface. In the measurement of the ARS pattern, the sample is tilted about 5 ° around the direction perpendicular to the rectangular ridge (X direction) and pinhole mask is set at the position corresponding to the surface normal direction (Z direction) [17,21]. This slightly tilts the incident beam direction from the surface normal direction, though it does not affect the symmetry in the X direction. The pinhole mask was moved from this position horizontally. This corresponds to limiting the radiation direction to be detected approximately in the plane (X-Z plane) formed by the direction perpendicular to the ridge and the surface normal direction. That is, the wavevector $\boldsymbol{K}$ of the emitted photons is always within the X-Z plane.

V. ANGULAR DISTRIBUTION OF SPP INDUCED RADIATION FROM 1D CAVITY

In order to explain the mechanism of the ARS pattern and the BSS image, we propose a simplified cavity model replacing the rectangular ridge with a single wall, setting the cavity length to L and the reflection coefficient of the side wall to $Re^{i\phi}$. When the SPP wave is reflected by the side wall, a part of it is converted into light. As shown in Fig. 7(a), the radiation efficiency from the sidewall in the direction of SPP progression side is $Se^{i\delta}$, and the efficiency radiated to the opposite side is $S'e^{i\delta'}$. Therefore $S = S'$ in the surface normal direction ($\theta = 0$) and $S(\theta) \neq S'(\theta)$ in the inclined direction. It was theoretically suggested that the radiation by a small ridge can be approximated by dipole radiation from a dipole formed in the ridge [15]. Considering the case that the electric dipole formed by the SPP reflection is nearly parallel to the surface plane, the direction of the dipole arising on the right side is opposite to that of the left side, so the phase difference π exists between these radiations. When an electron is incident on position X in the cavity, the excited SPPs propagate in the positive and negative directions of the X axis and are reflected by the side walls. Consequently radiations with amplitudes of

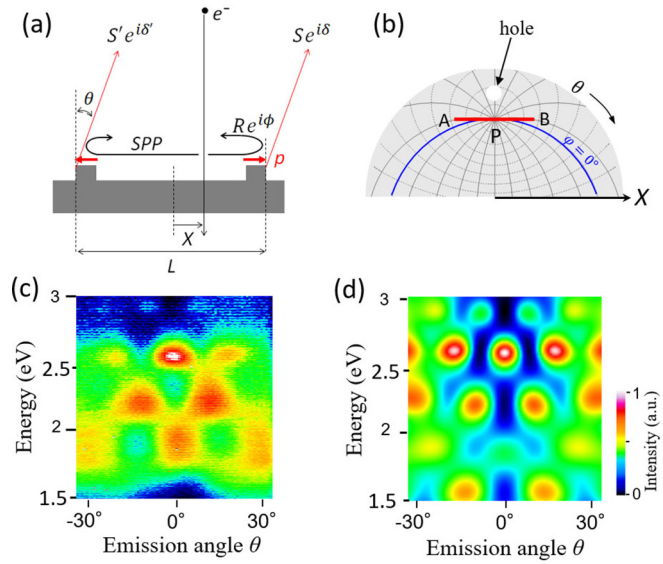

FIG. 7. (a) Schematic diagram of SPP reflection and simultaneous radiation from the ridges in the 1D cavity. (b) Projection of polar coordinates of the tilted sample onto the parabolic mirror and pinhole movement trajectory for ARS measurement (line AB). (c) Observed ARS pattern from the cavity and (d) simulated ARS pattern.

ψ^+ and ψ^- are generated, respectively. In addition, transition radiation ψ_{TR} which is generated when electrons are incident on the metal surface is added to this [31,32]. By taking the sum of these, the amplitude of total radiation from the cavity is expressed by the following equation:

$$\begin{aligned}\psi &= \psi^+ + \psi^- + \psi_{\mathrm{TR}} \\ &= T(\theta)e^{-i\omega t} + 2B[e^{-ik_pX}(Se^{i\delta} - S'e^{i\delta'}Re^{i[(k_p - K\sin\theta)L+\phi]}) \\ &\quad - e^{ik_pX}(S'e^{i\delta'} - Se^{i\delta}Re^{i[(k_p - K\sin\theta)L+\phi]})] \\ &\quad \times \frac{1}{1 - R^2e^{2i(k_pL+\phi)}}e^{ik_p\frac{L}{2}}\, e^{-i\omega t}. \end{aligned} \tag{6}$$

Here, T and B are the transition radiation and the SPP excitation amplitude, respectively, K is the wave number of the emitted light, and θ is the emission angle measured from the surface normal direction.

The resonant energy of the standing wave mode in the cavity can be obtained from the ARS pattern. The phase shift ϕ associated with the SPP reflection can be extracted through the cavity condition of Eq. (1) using the wave number k_p corresponding to the resonant energy. The cavity used for the experiment was composed of two ridges with a width (w) of 330 nm and a height (h) of 50 nm and was placed at a distance (d) of 870 nm so that the cavity length L became 1530 nm. The pinhole mask was scanned along the line AB in Fig. 7(b) so as to intersect the surface normal direction (P) to obtain the ARS pattern in Fig. 7(c). The bright spotlike contrasts appear at the energies of 1.93, 2.21, and 2.55 eV. The bright contrast appearing at $\theta = 0$ corresponds to radiation by an antisymmetric standing wave (n = odd) mode with a node at the cavity center, while the other one corresponds to a symmetric standing wave (n = even) mode with an antinode at the center. It is known that the wave number of SPP in the cavity follows the dispersion relation of

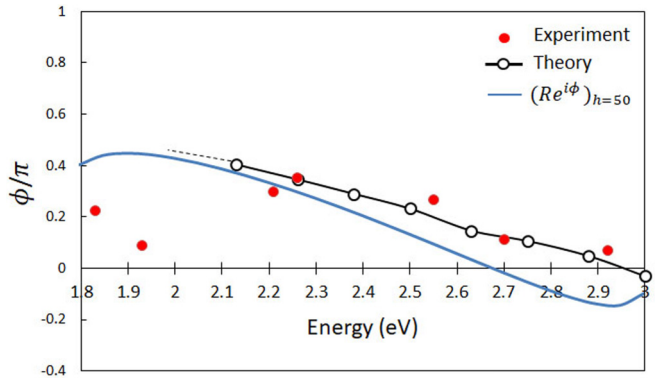

FIG. 8. Phase shift of the reflected SPP as a function of energy: open circles are the calculated values of Fig. 2 and red solid circles are experimental values derived from the ARS patterns of the cavities. The ridge width is 330 nm in the experiment and 325 nm in the calculation, respectively. The blue line indicates the phase shift of $(Re^{i\phi})_{h=50}$ at $w = 325$ nm.

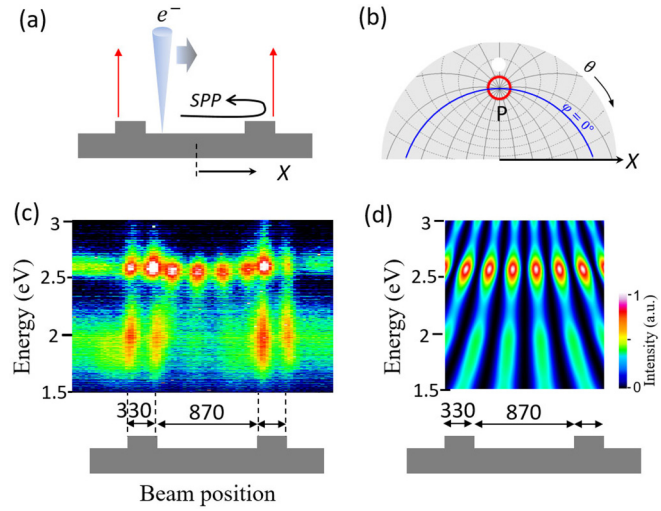

FIG. 9. (a) Schematic diagram of the BSS image measurement, and (b) pinhole mask position (red circle) on the parabolic mirror image. (c) BSS image taken using the radiation in the surface normal direction. (d) Simulated image calculated using Eq. (7).

SPP propagating on a flat silver surface [21]. Using the SPP dispersion relation of silver surface, the corresponding wave number k_p of each energy is obtained, and we found from the cavity condition that $n = 5$, 6, and 7 for the observed cavity modes. At the same time, from these values of n, the phase shifts at these energies $E_5, E_6,$ and E_7 are obtained to be $\phi_5 = 0.089\pi$, $\phi_6 = 0.30\pi$, and $\phi_7 = 0.27\pi$.

The relation between the phase shift and energy with the 330-nm ridge width thus obtained is plotted in red dots in Fig. 8. Values obtained from other cavities with the same ridge width and different cavity lengths are also plotted. For comparison, a plot of the theoretical value at $w = 325$ nm extracted from Fig. 2 is shown by an open circle in Fig. 8. Experiments and theoretical plots show good agreement with each other. This result proves that the theoretical calculation of the SPP reflection coefficient obtained in Sec. II is sufficiently correct. Therefore this ensures the validity of using the approximate function $(Re^{i\phi})_{h=50}$ of Eq. (5) as the reflection coefficient. The phase shift of $(Re^{i\phi})_{h=50}$ at $w = 325$ nm is indicated by the blue line in Fig. 8. The deviation of this function from the theoretical phase shift and the observed one is about 0.1π or less in the energy range of 2 to 3 eV. A simulated ARS pattern is shown in Fig. 7(d) that is calculated by using Eq. (6) with $(Re^{i\phi})_{h=50}$ and the other appropriate parameters. The radiation intensity depends on the beam position and is integrated over the cavity to compare to the observed ARS pattern. It is seen that the simulation pattern is in good agreement with the experimental result in Fig. 7(c). The characteristics of strong contrast such as the bright dots in the ARS pattern are mainly determined by the reflection coefficient $(Re^{i\phi})_{h=50}$.

Here we mention the other parameters used for the simulation, i.e., $T(E,\theta)$, $B(E)$ and $S(E,\theta)$, which give a broad background contrast of the ARS pattern. The transition radiation is polarized parallel to the reflection plane, the expression of which is given in Refs. [31,32]. The angular distribution can be approximated as $T(\theta) \propto \sin\theta\cos\theta$, so T is zero at $\theta = 0^\circ$ and is maximum around $\theta = 45^\circ$. Also, the intensity decreases approximately in inverse proportion to E as the energy E increases [17]. The excitation amplitude B of SPP is determined from the theory of electron energy loss spectroscopy (EELS) [33]. On bulk silver surfaces, B has a broad maximum over the range of 2.0 to 2.5 eV. As for the radiation S by the ridge, since the ridge width is close to 300 nm, referring to the result of Ref. [15,27], $S(\theta)$ can be approximated by the dipole radiation of the dipole tilted by a small angle α from the surface. That is, $S(\theta) \propto \sin^2(\theta + \pi/2 + \alpha)$, and $S'(\theta) = S(-\theta)$. The phases of $S(\theta)$ and $S'(\theta)$ are taken as $\delta(\theta) = \delta'(\theta)$ because the radiations are from the same type of oscillator to the directions of θ and $-\theta$. Then, the radiation by S becomes maximum at $\theta = \pm\alpha$. Since T, B, and S are slowly changing functions with respect to energy in the relevant energy range, the energy dependencies of T, B, and S were ignored for simplicity in the simulation. Also, it was found from the actual calculation that the phase difference between BS and transition radiation T has little effect on the ARS pattern. The smaller the BS/T, the weaker the contrast of the ARS pattern. After all, only two parameters are required for the simulation, which is BS/T and α. We set these parameters as $BS/T = 0.4$ and $\alpha = \pi/9$ to match the observed ARS pattern [Fig. 7(c)], and use them also for the other simulation.

The BSS image using radiation in the surface normal direction reflects the real space distribution of the SPP standing wave in the cavity. As schematically shown in Fig. 9(a), the BSS image was obtained by detecting radiation in the surface normal direction while scanning the electron beam across the cavity. The red circle in Fig. 9(b) represents the radiation angle range detected by the pinhole mask around the position P on the mirror corresponding to the surface normal direction. The measured BSS image is shown in Fig. 9(c). Only standing waves in the antisymmetric mode ($n =$ odd) contribute to this BSS image. There are five nodes in the contrast of energy E_5, which means that $n = 5$ mode, and similarly the contrast of E_7 with seven nodes means $n = 7$ mode. Both are antisymmetric standing waves with nodes at the center. It was confirmed that

the spacing between nodes in the inner planer region of the cavity coincides with the half period of the SPP wavelength derived from the dispersion relation of the SPP propagating on the flat surface. This is the same as the case of the cavity of a one-dimensional plasmonic crystal [21].

Using $T(0) = 0$ and $Se^{i\delta} = S'e^{i\delta'}$ for $\theta = 0$, Eq. (6) can be rewritten as

$$I_{\mathrm{BSS}}(X) = \left| 2BS \left(\frac{1}{1-R} \right) \sin k_p X \right|^2. \tag{7}$$

This expression represents the square modulus of the z component of the electric field of the cavity eigenstate on the surface, $|E_z|^2$, or the electromagnetic local density of states projected on the electron trajectory (z axis) (zEMLDOS) [34–36]. However, this equation cannot be applied near the steps at both sides of the ridge because of the complex electric field distribution near the step. It can be seen from Eq. (7) that the intensity of the BSS image becomes stronger as the amplitude R becomes closer to 1. From the results in Fig. 2(a), at the ridge width of 325 nm, R is as small as 0.1 at $E_5 = 1.93$ eV and as large as 0.4 at $E_7 = 2.55$ eV. Correspondingly, it can be confirmed that the contrast in the inner region between the two ridges is weak at E_5 and strong at E_7 . However, the contrast of E_5 is strong at the step on the side of the ridge. This strong radiation is considered to be due to the local standing wave formed on the ridge. Looking at the intensity distribution of the contrast of the standing wave of E_7 in detail, the spacing between the antinodes of the contrast changes discontinuously at the inner up step. In addition, the outer down step is not completely located at the position of the antinode. These contrasts clearly reveal the spatial distribution of the phase of the standing waves in the cavity and give the validity to introduce the parameters of ηh and ϕ_d to the reflection coefficient. Figure 9(d) shows a simulated BSS image calculated by Eq. (7) where the same parameters as in Fig. 7(d) were used. The intensity distribution in the cavity is well reproduced in the simulated image except near the steps.

Finally, we examined the range of sizes of the cavities in which the above model approximating the ridge as a single wall is valid. Cavities with varying width L were used, of which ridge height is 70 nm and ridge widths are (a) $w = 265$ and (b) 337 nm. Figures 10(a) and 10(b) show the ARS patterns from these cavities. The corresponding simulation patterns are presented under each ARS pattern. Regarding the parameters for the simulation, we used the reflection coefficient $(Re^{i\phi})_{h=70}$ mentioned in Sec. III and the same values of α and BS/T as before.

When the cavity length is larger than 1000 nm, there is a slight difference in the intensity distribution between the observed and simulated ARS patterns, but a good match is obtained. Therefore this means that the model we used is valid for $L > 1000$ nm at $w \sim 300$ nm. For $L < 1000$ nm, the simulation results cannot well reproduce the observed ARS pattern. In this case, the distance between the ridges is of the same order as the ridge width so that the radiation from the cavity cannot be approximated as the interference of the dipole radiations from the two ridges. In this small L region, the radiation intensity is occasionally enhanced as seen in the pattern of $L = 857$ nm in Fig. 10(a). To find such enhancement

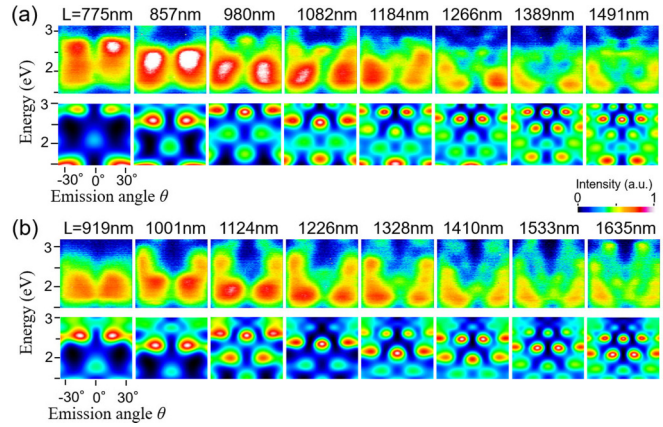

FIG. 10. ARS patterns from 1D-cavities with different cavity length. Simulated pattern is under each ARS pattern. The ridge height is 70 nm and the ridge widths are (a) $w = 265$ and (b) 337 nm, respectively.

condition can be important to the application, so a further theoretical approach is expected.

VI. CONCLUSION

Reflection characteristics of surface plasmon polariton (SPP) by rectangular ridge on silver surface were investigated from theory and experiment. The amplitude and phase shift of the reflection by the ridge were calculated by the SPP scattering theory using the Green's tensor method for various ridge widths and energies. This theoretical result can be well reproduced by a simple model expressing the superposition of reflections by the two steps constituting the ridge. The parameters in the expression of the reflection coefficient are properly determined to fit the theoretical curves, and two-dimensional maps representing $R(E, w)$ and $\phi(E, w)$ are obtained using these parameters. The SPP radiation characteristics from the cavity consisting of rectangular ridge pairs was clarified for the first time using the STEM-CL method and was used to evaluate the theoretical calculations of the reflection coefficient. It was confirmed that the amplitude and phase shift of the ridge reflection of the SPP standing wave satisfying the cavity condition are in good agreement with the theoretical ones. The simulation of the ARS pattern using the simple model of the reflection coefficient agreed well with the experimental result. However, this treatment is valid for the cavity whose inner distance d between the ridges is sufficiently larger than the ridge width w. The present results indicate that the STEM-CL method is a powerful tool for studying the radiation characteristics of the plasmonic cavity and the nature of the SPP standing wave mode (cavity mode). These results can provide useful information in the design of nanoplasmonic devices using rectangular ridges such as cavities.

ACKNOWLEDGMENTS

The authors thank F. J. García de Abajo for fruitful discussion on cavity radiation. This work was partly supported by Tokyo Institute of Technology in "Nanotechnology Platform Project No. 120250214" sponsored by the Ministry of Education, Culture, Sports, Science and Technology (MEXT), Japan.

[1] H. Raether, *Surface Plasmons on Smooth and Rough Surfaces and on Gratings*, Springer Tracks in Modern Physics Vol. 111 (Springer-Verlag, Berlin, 1988).

[2] S.A. Maier, *Plasmonics: Fundamentals and Applications* (Springer, New York, 2007).

[3] P. Berini and I. De Leon, Nat. Photonics **6**, 16 (2012).

[4] J. T. Hugall, A. Singh, and N. F. van Hulst, ACS Photonics **5**43 (2018).

[5] W. L. Barnes, A. Dereux, and T. W. Ebbesen, Nature (London) **424**, 824 (2003).

[6] D. K. Gramotnev and S. I. Bozhevolnyi, Nat. Photon. **4**, 83 (2010).

[7] A. V. Zayats, I. I. Smolyaninov, and A. A. Maradudin, Phys. Rep. **408**, 131 (2005).

[8] H. A. Jamid and S. J. Al-Bader, IEEE Photonics Technol. Lett. **9**, 220 (1997).

[9] N. Yamamoto and T. Suzuki, Appl. Phys. Lett. **93**, 093114 (2008).

[10] N. Yamamoto, in *The Transmission Electron Microscope*, edited by M. Khan (InTech, Croatia, 2012), Chap. 15, pp. 1–24.

[11] A. Sanchez-Gil and A. A. Maradudin, Opt. Express **12**, 883 (2004).

[12] M. Kuttge, F. J. García de Abajo, and A. Polman, Opt. Express **17**, 10385 (2009).

[13] J. A. Sánchez-Gil and A. A. Maradudin, Phys. Rev. B **60**, 8359 (1999).

[14] M. Kuttge, E. J. R. Vesseur, and A. Polman, Appl. Phys. Lett. **94**, 183104 (2009).

[15] G. Brucoli and L. Martin-Moreno, Phys. Rev. B **83**, 045422 (2011).

[16] G. Brucoli and L. Martin-Moreno, Phys. Rev. B **83**, 075433 (2011).

[17] N. Yamamoto, Microscopy **65**, 282 (2016).

[18] H. Watanabe, M. Honda, and N. Yamamoto, Opt. Express **22**, 5155 (2014).

[19] N. Yamamoto and H. Saito, Opt. Express **22**, 29761 (2014).

[20] H. Saito and N. Yamamoto, Opt. Express **23**, 2524 (2015).

[21] M. Honda and N. Yamamoto, Opt. Express. **21**, 11973 (2013).

[22] H. Saito and N. Yamamoto, Nano Lett. **15**, 5764 (2015).

[23] H. Saito, S. Mizuma, and N. Yamamoto, Nano Lett. **15**, 6789 (2015).

[24] H. Saito, N. Yamamoto, and T. Sannomiya, ACS Photonics **4**, 1361 (2017).

[25] J.-C. Weeber, Y. Lacroute, and A. Dereux, Phys. Rev. B **68**, 115401 (2003).

[26] W. C. Chew, *Waves and Fields in Inhomogeneous Media* (Wiley-IEEE Press, New York, 1999).

[27] Giovanni Brucoli, Ph.D. thesis, CSIC-University de Zaragoza, 2010.

[28] O. J. F. Martin, A. Dereau, and C. Girard, Opt. Soc. Am. A **11**, 1073 (1994).

[29] O. J. F. Martin, C. Girard, and A. Dereux, Phys. Rev. Lett. **74**, 526 (1995).

[30] P. B. Johnson and R.W. Christy, Phys. Rev. B **6**, 4370 (1972).

[31] V. L. Ginzburg and I. M. Frank, Zh. Eksp. Teor. Fiz. **16**, 15 (1946) [J. Phys. **9**, 353 (1946)].

[32] M. L. Ter-Mikaelian, *High-Energy Electromagnetic Processes in Condensed Media* (Wiley, New York, 1972).

[33] E. Kröger, Z. Phys. **216**, 115 (1968).

[34] G. C. des Francs, C. Girard, J.-C. Weeber, C. Chicane, T. David, A. Dereux, and D. Peyrade, Phys. Rev. Lett. **86**, 4950 (2001).

[35] F. J. García de Abajo, Rev. Mod. Phys. **82**, 209, (2010).

[36] M. Kociak and F. J. García de Abajo, MRS Bulletin **37**, 39 (2012).